Effect of Finger Orientation on Contact Stiffness and Area During Sliding on a Smooth Surface

by

Jahangier Ahmad

A Dissertation Submitted to the
Graduate School of Sciences and Engineering
in Partial Fulfillment of the Requirements for
the Degree of

Master of Science

in

Mechanical Engineering

KOÇ ÜNİVERSİTESİ

October 3, 2024

Effect of Finger Orientation on Contact Stiffness and Area During Sliding on a Smooth Surface

Koç University

Graduate School of Sciences and Engineering

This is to certify that I have examined this copy of a master's thesis by

Jahangier Ahmad

and have found that it is complete and satisfactory in all respects,

and that any and all revisions required by the final

examining committee have been made.

Committee Members:

Prof. Dr. Çağatay Başdoğan (Advisor)

Prof. Dr. Murat Sözer (Koc Univ.)

Assoc. Prof. Evren Samur (Bogazici Univ.)

Date: ______________________

To my parents, wife, and kids!

ABSTRACT

Effect of Finger Orientation on Contact Stiffness and Area During Sliding on a Smooth Surface
Jahangier Ahmad
Master of Science in Mechanical Engineering
October 3, 2024

Earlier experimental studies showed that the apparent contact area of human fingerpad shrinks and eventually reaches a steady-state value as it slides on a smooth surface, although the root causes of this reduction have not been fully understood yet. In this thesis, we hypothesize that finger rotation about its axial axis and the movement direction play critical roles in the area change. To test this hypothesis, we conducted an experimental study to investigate the evolution of apparent contact area between human fingerpad and a smooth flat surface under normal loading (stationary finger) and combined loading (sliding finger) conditions for 4 different internal rotations of the index finger about its axial (longitudinal) axis and 2 different sliding directions (radial and ulnar). Our results show a reduction in the contact area for radial sliding as expected, but a surprising increase in the ulnar direction for the higher finger rotations. We argue that this asymmetric behavior in contact area evolution stems from the changes in the equivalent radius of curvature and stiffening of the finger as the rotation angle increases, which manifests itself as the asymmetric stress distribution at the leading and trailing edges of the fingerpad in our finite element simulations.

ÖZETÇE

Pürüzsüz bir Yüzey Üzerinde Kayan İnsan Parmağının Oryantasyonunun Kontak Sertliğine ve Alanına Etkisi
Jahangier Ahmad
Makine Mühendisliği, Yüksek Lisans
03 Ekim 2024

Daha önceki deneysel çalışmalar insan parmağının görünür temas alanının pürüzsüz ve düz bir yüzey üzerinde kayarken küçüldüğünü ve sonunda sabit bir değere ulaştığını göstermiştir, ancak bu küçülmenin temel nedenleri henüz tam olarak anlaşılamamıştır. Bu tez çalışmasında, parmağın uzun ekseni etrafında dönmesinin ve kayma yönünün kontak alanına etkisi olduğunu varsayıyoruz. Bu hipotezi test etmek amacıyla, işaret parmağının 4 farklı iç rotasyonu ve 2 farklı kayma yönünü (radyal ve ulnar) için normal yükleme (sabit parmak) ve birleşik yükleme (kayan parmak) koşulları altında parmağın görünür temas alanının değişimini araştırmak için deneysel bir çalışma gerçekleştirdik. Sonuçlarımız, beklendiği gibi, radyal yönde kayma için temas alanında bir azalma olduğunu ancak yüksek parmak rotasyonları için ulnar yönde şaşırtıcı bir artış olduğunu göstermektedir. Temas alanı değişimindeki bu asimetrik davranışın, dönme açısı arttıkça, parmağın eşdeğer eğrilik yarıçapındaki değişimden ve parmağın sertleşmesinden kaynaklandığını, ve bunun da yaptığımız sonlu eleman simülasyonlarında, parmağın ön ve arka kenarlarındaki asimetrik gerilim dağılımı olarak kendini gösterdiğini savunuyoruz.

ACKNOWLEDGMENTS

I express my profound gratitude to Prof. Dr. Çağatay Başdoğan for bestowing upon me the invaluable opportunity to delve into an emerging realm of research - the intricate investigation of mechanics of human fingerpad contact with smooth surfaces. I extend my heartfelt thanks to all my esteemed colleagues at the Robotics and Mechatronics Laboratory (RML). I am especially indebted to EasaAli Abbasi for his exceptional mentorship and steadfast support during the crucial phase of conducting experiments and compiling the results. His expertise has been a guiding light that led me through any challenges encountered along the way. Last but not least, I am profoundly grateful to my cherished friends and beloved family, particularly my loving wife and children. Their unwavering encouragement and understanding have been the pillars of strength that sustained me throughout this endeavor.

TABLE OF CONTENTS

LIST OF TABLES

LIST OF FIGURES

ABBREVIATIONS

CoF	Coefficient of Friction
FEM	Finite Element Modeling
PID	Proportional-Integral-Derivative
SC	Stratum Corneum

Chapter 1

INTRODUCTION

1.1 Context

Contact mechanics between a human fingerpad and a smooth surface has captured the interest of researchers due to its potential applications in various domains such as haptics (enabling tactile effects by modulating the interaction forces between the human finger and touch surface), tribology (study of friction, lubrication, and wear) and robotics [Basdogan et al., 2020, Derler and Gerhardt, 2012, Babin and Gosselin, 2021]. Contact mechanics involved in the tactile perception of surfaces and the graspability of human fingerpads are significantly influenced by a combination of factors, including surface roughness, material properties, contact area, pressure distribution, and amount and frequency of finger deformation [van Kuilenburg et al., 2015]. These elements play a crucial role in how we sense and interact with objects, impacting our ability to perceive textures, handle objects comfortably, and maintain a secure grip [Kishishita et al., 2021].

The macroscopic deformation of the human finger during exploration of surfaces produces local stretching and compression at the axon membrane bi-layer, which generates a remarkable amplification of the mechanoelectrical signals carrying the tactile information of the fingerpad's contact interface with a surface [Somer et al., 2015]. On the other hand, in object grasping, stability is achieved by coordinated changes in the magnitude of normal and tangential forces [Burstedt et al., 1997a, Burstedt et al., 1997b]. Humans perform both operations by adjusting the frictional forces, and the real contact area (A_{real}) dominantly influences the tangential forces acting on the finger [Adams et al., 2007]. The force of friction (F_t) remains unaffected by the apparent contact area (A_{app}) and comprises two primary constituents. The first involves adhesion, arising from attractive forces within the real contact area, which is smaller than the apparent contact area (see Figure 1.1a to c), while the second pertains to deformation – the force essential for ploughing the micro-irregularities in contact [Bowden and Tabor, 1964].

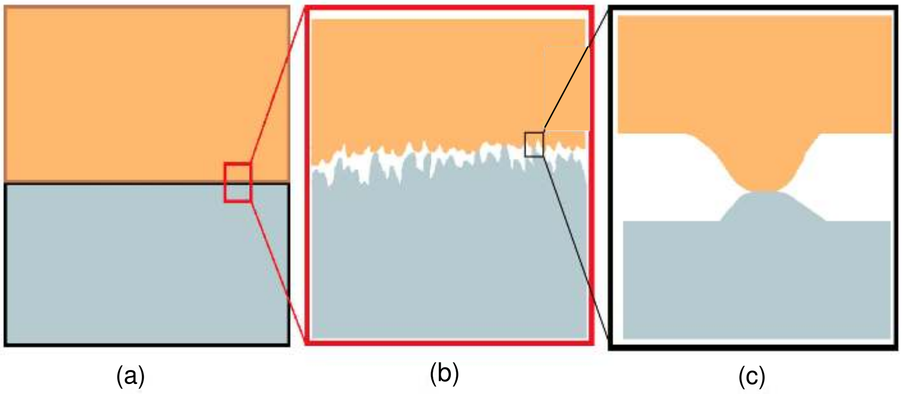

Figure 1.1: Real contact area is a fraction of apparent contact area (a) Apparent contact area between two surfaces, (b) Real contact area comprised of multiple asperities, and (c) Single asperity contact which can be modeled as a sphere-plane contact.

Although, the mechanoreceptors are responsible for converting the specific skin deformations into signals, but it is the collective input from multiple tactile fibers spread across a wider area of the skin that allows us to interpret the characteristics of the interface between the skin and the surface of the manipulated object [Corniani et al., 2022]. Moreover, as the contact is buried between the two bodies, it is challenging to accurately measure the real contact area and to understand its dependence on the normal load and material properties of the contacting bodies [Jacobs and Martini, 2017].

Therefore, investigating the influence of different factors such as the normal and tangential forces, finger orientation, and sliding direction on the evolution of the apparent contact area, when a fingerpad interacts with a flat surface, is a valuable endeavor. Comprehending the mechanics of human finger contact presents a formidable challenge, necessitating the application of advanced mathematical methodologies due to the intricate interplay between normal (F_n) and tangential (F_t) forces during sliding. This challenge is compounded by the finger's intricate morphological structure, hyper-viscoelastic material properties, and physiological characteristics. Nonetheless, numerous research studies have demonstrated that Hertzian contact theory can effectively anticipate changes in the apparent contact area in response to varying normal forces, often conforming to a power law relationship with an exponent less than or equal to 2/3.

1.2 Contact mechanics for normal loading of the fingerpad

During stationary contact with a smooth surface under normal loading, the apparent contact area of fingerpad (A_{app}) increases non-linearly with the applied normal force, which can be estimated by the Hertz contact model [Persson, 2006]. Johnson, Kendall, and Roberts (JKR) [Johnson et al., 1971] improved the Hertz contact model by considering the adhesive interactions due to van der Waals forces. They estimated a greater contact area compared to the Hertzian prediction for a given normal force and showed that there exists a finite contact area even at zero normal force due to adhesion. In comparison to JKR theory, Derjaguin, Muller, and Toporov (DMT) [Derjaguin et al., 1975], considered multiple contact points and accounted for both elastic and non-elastic deformations due to adhesive forces. Tabor [Tabor, 1977] conducted further research and demonstrated that the JKR and DMT theories are specific scenarios within a broader framework that incorporates adhesion forces both inside and outside the contact region and concluded that adhesion between solids depends not only on surface forces but also on surface roughness and degree of ductility of the solids themselves.

To consider the surface roughness, Greenwood and Williamson [Greenwood and Williamson, 1966] assumed that the asperities of the rough surface in contact with a smooth surface vary randomly with some probabilistic distribution and the Hertz contact model is applicable for each asperity to calculate the total contact area. Persson [Persson, 2001] extended this probabilistic approach by considering the surface roughness at multiple length scales in which the asperities are of different heights and radii of curvature. In this approach, the real area of contact (A_{real}) is predicted to be much smaller than the apparent contact area [Persson et al., 2013] contingent upon factors such as the normal force, moisture level, and the duration of contact [Adams et al., 2007]. For example, hydration (increase in moisture level) increases the apparent finger contact area due to the softening of the finger, also known as plasticization [Adams et al., 2007], and the ratio of real to apparent contact areas [Serhat et al., 2022].

The earlier studies also showed that the material properties of the finger significantly influence the contact area. The human skin comprises multiple layers with different material properties, resulting in nonlinear and time-dependent responses to the combined normal and tangential loading [Gray, 1878, Fawcett, 1986, WA, 1994, Rubin et al., 1998]. Dzidek et al. [Dzidek et al., 2017] proposed an elastic contact model based on a geometrical simplification of the fingerpad in which its secant modulus was found linearly proportional to the normal force. The results of their experiments, performed under normal loading up to 2 N, showed higher values of apparent contact area for a stationary finger inclined at 30° with respect to a glass plate compared to that of 45°. Whereas, Young's modulus and the secant modulus of the fingerpad were reported higher for the 45° inclination than those of 30°.

1.3 Contact mechanics for combined normal and tangential loading of the fingerpad

In contrast to normal loading, contact mechanics of human finger sliding on a smooth surface under combined loading of normal and tangential forces has been investigated less in the literature since it is a more complex problem. The mechanisms contributing to the sliding friction include adhesion, deformation of asperities, plastic deformation at the contact interface, fracture, interlocking, finger moisture, and the contamination particles between the surfaces [Nosonovsky and Bhushan, 2007, Pasumarty et al., 2011, Derler and Gerhardt, 2012, Adams et al., 2013]. In particular, the experimental studies show that the adhesion plays an important role in finger friction during contacts with a smooth surface [Maegawa et al., 2015, Basdogan et al., 2020]. [Mergel et al., 2019] found that when a smooth glass plate slides on a PDMS sphere under low loads, the contact area decreases with the friction force. They observed that the ratio F_t/A_{real} increases linearly until reaching a maximum friction force, after which it stabilizes. This suggest that assuming constant shear stress during sliding is reasonable for modeling adhesion-controlled friction, where $F_t = \tau_0 A_{real}$ where τ_0 is interfacial shear stress. [Sahli et al., 2019] investigated anisotropic shearing of the contact area due to tangential force via a fracture mechanics model. They showed that in rough elastomer contacts, the shape of microjunctions changes significantly in response to the shear force applied to the interface. This results in increasing anisotropy of the overall contact interface, which eventually stabilizes in the macroscopic sliding regime. Additionally, the contact areas of these microjunctions evolve differently over time, suggesting distinct behaviors of individual tangential forces. [Scheibert et al., 2020] speculates that these variations may result from tangential elastic interactions between microjunctions.

[Xu et al., 2022] modeled the adhesive friction behavior of a linear elastic rough contact interface using independent spherical asperities, treating their peripheries as interfacial cracks under mixed mode loading. Their model effectively captures shear-induced reduction of the real contact area, attributed to junction shrinkage, and predicts a static friction peak at the macroscale. It shows that both the static friction peak and contact area evolution depend on normal load and key microscale properties, such as surface energy, mode mixity, and frictional shear strength. They show that a tougher interface (higher surface energy, lower mode mixity) results in greater contact area and a more pronounced static friction peak, particularly at lower normal loads. Conversely, the peak can "disappear" with higher frictional shear strength and a weaker interface. The friction coefficient is higher for the contacts with a smooth surface at low normal forces but reduces as the normal force is increased [Derler et al., 2009]. Moreover, the frictional behavior of human finger contacts is influenced by the sliding direction. When sliding on sandpaper at a velocity of $20 mm/sec$, the human finger exhibited a higher coefficient of friction in the proximal direction compared to the distal direction [Zhou et al., 2020].

Moreover, the earlier studies also show that the apparent contact area of the fingerpad reduces during sliding with the increase in tangential forces until reaching a steady-state value [Delhaye et al., 2014, Sahli et al., 2018, Sirin et al., 2019]. [Delhaye et al., 2014] measured the contact area between sliding human finger and a flat glass surface for 3 normal forces (0.5, 1, and 2 N) and 3 sliding velocities (5, 10, and 20 mm/s) along 4 anatomical directions (distal, proximal, radial, and ulnar). They reported a reduction of approximately 30% in the apparent contact area for all directions. Similar results were also reported by [Sahli et al., 2018] for the contacts between a sliding human finger and a smooth surface. They showed that the reduction in contact area starts with the application of tangential forces and saturates well before macroscopic sliding. This suggests that assuming constant shear stress during sliding is reasonable for modeling adhesion-controlled friction [Mergel et al., 2019]. [Sahli et al., 2019] investigated anisotropic shearing of the contact area due to tangential force via a fracture mechanics model. They showed that in rough elastomer contacts, the shape of microjunctions changes significantly in response to the shear force applied to the interface. This results in increasing anisotropy of the overall contact interface, which eventually stabilizes in the macroscopic sliding regime.

Despite the experimental evidence, the contact mechanics behind the reduction in the apparent contact area of the sliding finger is still not fully understood. Adhesion models based on linear elastic fracture mechanics has been utilized to interpret the anistropic area reduction. Savkoor and Briggs [Savkoor and Briggs, 1977] expanded upon the JKR theory by incorporating tangential forces into their analysis. Their research revealed that when subjected to increasing tangential loads, the contact area between a sphere and a half-space actually decreases. However, it's important to note that their model did not consider frictional resistance, which led to an underestimation of interfacial toughness and an overestimation of the reduction in contact area. To address this limitation, subsequent studies have recognized the significance of friction and plasticity in enhancing interfacial toughness, especially when dealing with combination of mode-I (opening crack) and mode-II (shearing crack) in contacts under the effect of tangential loading [Hutchinson et al., 1990]. In this regard, researchers have introduced an empirical Mode-Mixity Function to better account for the effects of mode combination on area reduction [Papangelo et al., 2019]. Researchers have proposed adhesionless models based on hyperelasticity principles to address substantial deformations in elastomer contacts, with a prominent application being in scenarios like fingerpad interactions with a glass plate [Mergel et al., 2021, Wang et al., 2020]. It has been argued that the nonlinear material properties of the finger and stiffening in the direction of sliding also play an important role in area reduction [Delhaye et al., 2014]. Moreover, [Lengiewicz et al., 2020] argued that the finite deformations govern the area reduction during sliding, with a dominating effect of local contact lifting at the trailing edge. [Mergel et al., 2021] developed a comprehensive computational framework for contact mechanics where adhesion and friction interact in a coupled manner. The model captures the dynamic interaction between these two forces, particularly in soft and elastic materials when in contact with smooth and flat surfaces. Their results indicate that shear-induced area reduction in these interfaces is not limited to (nearly) incompressible materials. Furthermore, they suggest that while adhesion is not essential for modeling this phenomenon, it amplifies the effect resulting from finite, non-linear material deformations.

1.4 This work

We hypothesize that not only the nonlinear stiffening and finite deformations of the finger but also the finger rotation about its axial axis affects the contact area during sliding on a smooth surface. Finger contacts with surfaces in our daily activities frequently involve rotation angles beyond zero degrees. Instances of rotations higher than zero degrees are common when interacting with digital objects on the touchscreen of a cell phone, exploring the texture of a surface, or grasping and manipulating an object with multiple fingers. The earlier studies investigating the contact mechanics between the fingerpad and a smooth surface under normal or combined loading conditions mostly ignored the changes in contact area due to the rotation of finger. Moreover, when grasping a curved object or exploring an inclined surface under combined loading as presented in Figure 1.2a and b respectively, our fingers

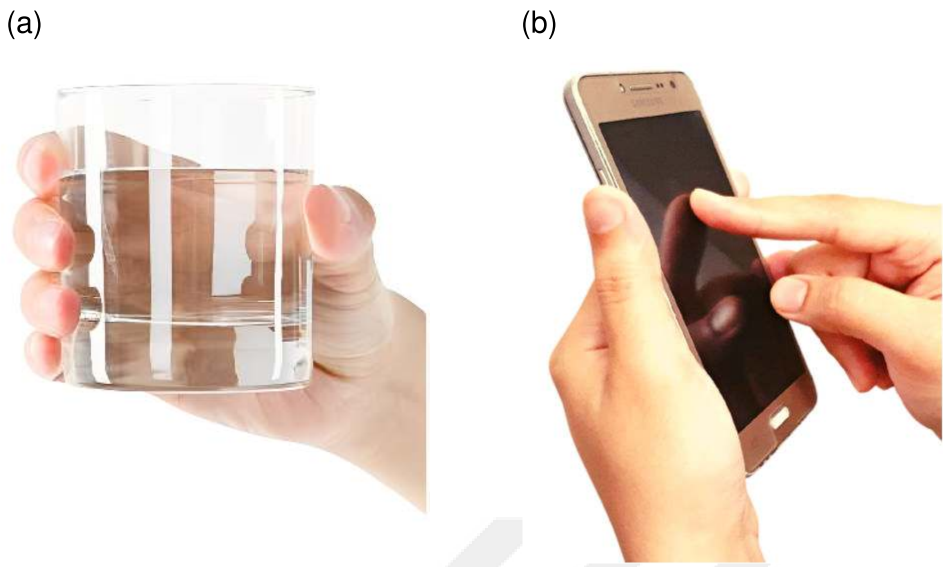

Figure 1.2: Human fingers can take different orientations when (a) grasping a curved object and (b) exploring a surface or sliding over a touchscreen. During the manipulation of an object, the human fingers apply and adjust normal force, whereas an inward rotation of the finger about the distal axis occurs as a result of the tangential force.

can take different orientations relative to the contacted surface, and the contact area may frequently change again.

Under the contact conditions above, the equivalent radius of curvature (R_e), one of the factors affecting the apparent contact area, changes with the finger orientation since the cross-section of the human finger is elliptical and not circular. The radius of the Hertizian circular apparent contact area between two objects is given by the following relation.

$$r_H = \left[\frac{3F_nR_e}{4E^*}\right]^{1/3} \tag{1.1}$$

Where E^* is the effective elastic modulus ($\frac{1}{E^*} = \frac{1-v_1^2}{E_1} + \frac{1-v_2^2}{E_2}$). E_1, E_2 are the elastic moduli, and v_1, v_2 are the Poisson's ratios of the contacting bodies i.e. fingertip and flat surface respectively.

The equivalent radius of curvature (R_e) of two curved bodies is calculated as $\frac{1}{R_e} = \frac{1}{R_1} + \frac{1}{R_2}$. where R_1 and R_2 are the radii of curvatures of the contacting bodies

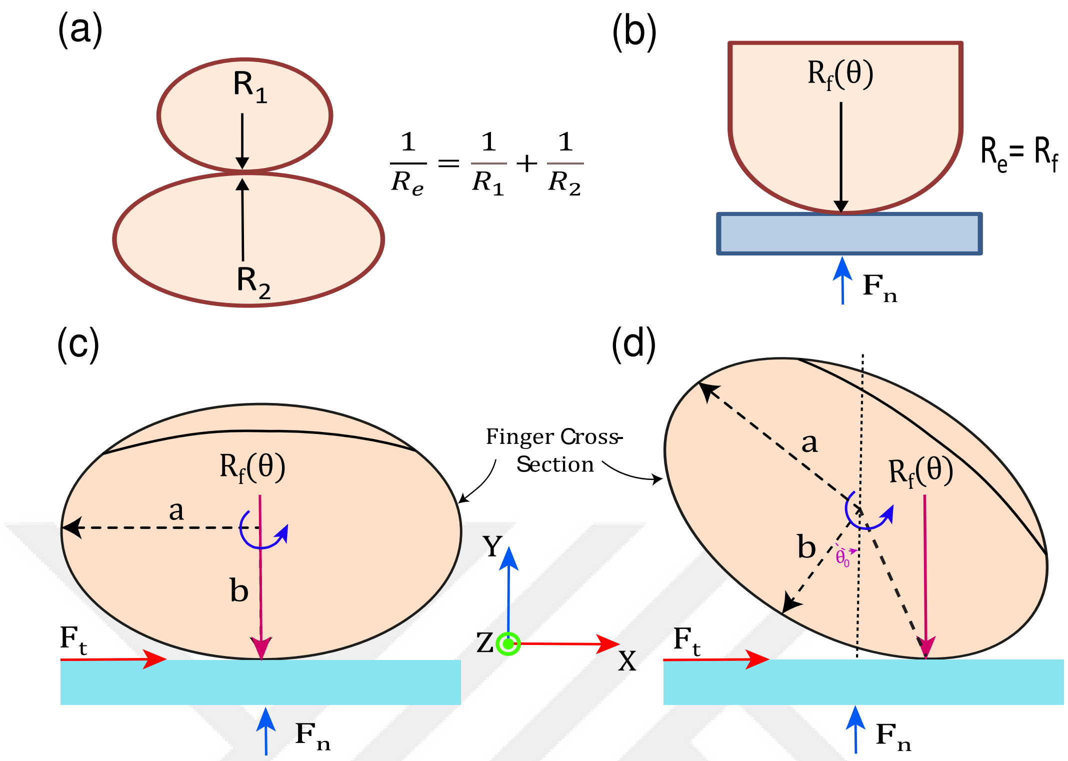

Figure 1.3: Equivalent radius of curvature R_e and apparent contact area (a) R_e of elliptical bodies with radii of curvatures R_1 and R_2, (b) radius of curvature of a flat surface is considered to be infinite therefore, R_e is equal to R_f in case of fingertip in contact with a flat surface, (c) elliptical fingertip cross-section for $\theta_0 = 0°$, and (d) $\theta_0 \neq 0°$ during ulnar sliding.

(Fig. 1.3a). Whereas, for fingertip in contact with a flat surface, R_e is equal to the radius of curvature of the fingertip cross-section (R_f) only (Fig. 1.3b). The radius of curvature of the elliptical fingertip geometry is a function of the rotation angle θ of the fingertip about its axial axis and can be estimated by the following relation.

$$R_f(\theta) = \frac{[(acos(\theta))^2 + (bsin(\theta))^2]^{3/2}}{ab} \tag{1.2}$$

Where a and b are major and minor radii of the elliptical cross-section of the fingertip as presented in Fig. 1.3c. Furthermore, the R_e changes due to the rotation of the finger about its distal axis under the effect of tangential load as shown in Fig. 1.3d.

Moreover, the human finger exhibits a complex hierarchical structure, comprising multiple sub-structures, each characterized by distinct material properties. As the orientation of the finger changes, stiffening may occur, which may again affect the contact area.

To test our hypothesis, we conducted an experimental study to investigate the effect of finger rotation about its axial axis on the evolution of the apparent contact area of fingerpad i) under normal loading and ii) under combined normal and tangential loading during sliding in ulnar and radial directions. The coefficient of sliding friction ($CoF = F_t/F_n$) was measured as a function of displacement under the sliding condition. To validate our experimental results and gain a deeper understanding of the contact mechanics between the human finger and a smooth surface, finite element modeling (FEM) simulations were performed in COMSOL Multiphysics for the conditions corresponding to our physical experiments. Our experimental and FEM results reveal a decrease in contact area for radial sliding, consistent with prior studies for the case of no rotation, $\theta_0 = 0°$ [Delhaye et al., 2014, Sahli et al., 2018]. However, for the internal finger rotations of $\theta_0 = 30°$ and $45°$, an increase in the contact area was observed for ulnar sliding.

To our knowledge, this is the first study in the literature reporting an increase in the apparent contact area for the sliding human finger. Additionally, we observed that steady-state CoF decreases with increased normal load, reflecting adhesion effects at low normal forces as reported in [Derler et al., 2009, Basdogan et al., 2020]. The stiffening of the finger with an increase in rotation angle also contributes to decreased steady-state CoF due to a drop in apparent contact area.

1.4.1 Contributions

The contributions of the present study to the current state of literature are as follows:

- the apparent contact area is reduced and the finger becomes stiffer as the rotation angle about its axial axis is increased under normal loading.

- change (increase/decrease) in apparent contact area is affected by the finger rotation about its axial axis for both ulnar and radial sliding direction. Our results show a reduction in the contact area for radial sliding as expected, but a surprising increase in the ulnar direction for the higher finger rotations. For the finger rotation of $\theta_0 = 15°$ about its axial axis, the apparent contact area remains almost constant.

- As the normal load increases, the steady-state coefficient of friction (CoF) decreases. This occurs because the finger becomes stiffer with a greater rotation angle, resulting in a reduced steady-state CoF.

The rest of the present study is organized as follows:

Chapter 2 explains the technical approach followed in the study, including the hardware setup, detail of experiments including the experimental protocol and conditions, information about the participants, and the methods used for data collection and processing. Chapter 2 also contains fingerpad area calculation method, and finite element modeling details. Chapter 3 presents the results of both experimental data and finite element simulations for normal and combined loading conditions.. Chapter 4 offers insights into the results obtained by the study and a comparison of results with earlier relevant studies in the literature. Chapter 5 provides conclusive remarks, as well as possible future directions.

Chapter 2

APPROACH

The approach followed in this study is to investigate the effect of finger rotation about its distal axis and the sliding direction on the evolution of the apparent contact area i) experimentally, and ii) using finite element modeling and simulations of the fingertip in contact with a smooth surface. Experiments were conducted for two conditions i) stationary finger under pure normal loading and ii) finger sliding over the smooth surface in ulnar and radial directions under combined normal and tangential loading. A 2D finite element model was developed in COMSOL Multiphysics which enables realistic simulation of the human fingertip contact with a smooth surface for the conditions corresponding to our physical experiments.

2.1 Hardware Setup

The experiments were conducted utilizing the setup devised in [Ozdamar et al., 2020, AliAbbasi et al., 2022], incorporating a customized 3D-printed finger-support mechanism for precise control over the internal rotation of the index finger about its longitudinal axis at four distinct angles ($\theta_0 = 0°$, $15°$, $30°$, and $45°$) relative to the surface of a touchscreen (SCT3250, 3M Inc.), as depicted in Figure 2.1a. The finger was positioned at a 20° inclination relative to the touchscreen surface using custom-designed finger, arm, and hand supports.

The setup is composed of the following major components:

- capacitive touchscreen (SCT3250, 3M Inc.) mounted on two linear translational stages. In this study, the touchscreen was not supplied with any electrical excitation and was utilized as a smooth glass surface, and thus will be referred to as the "plate" in the remainder of this manuscript.

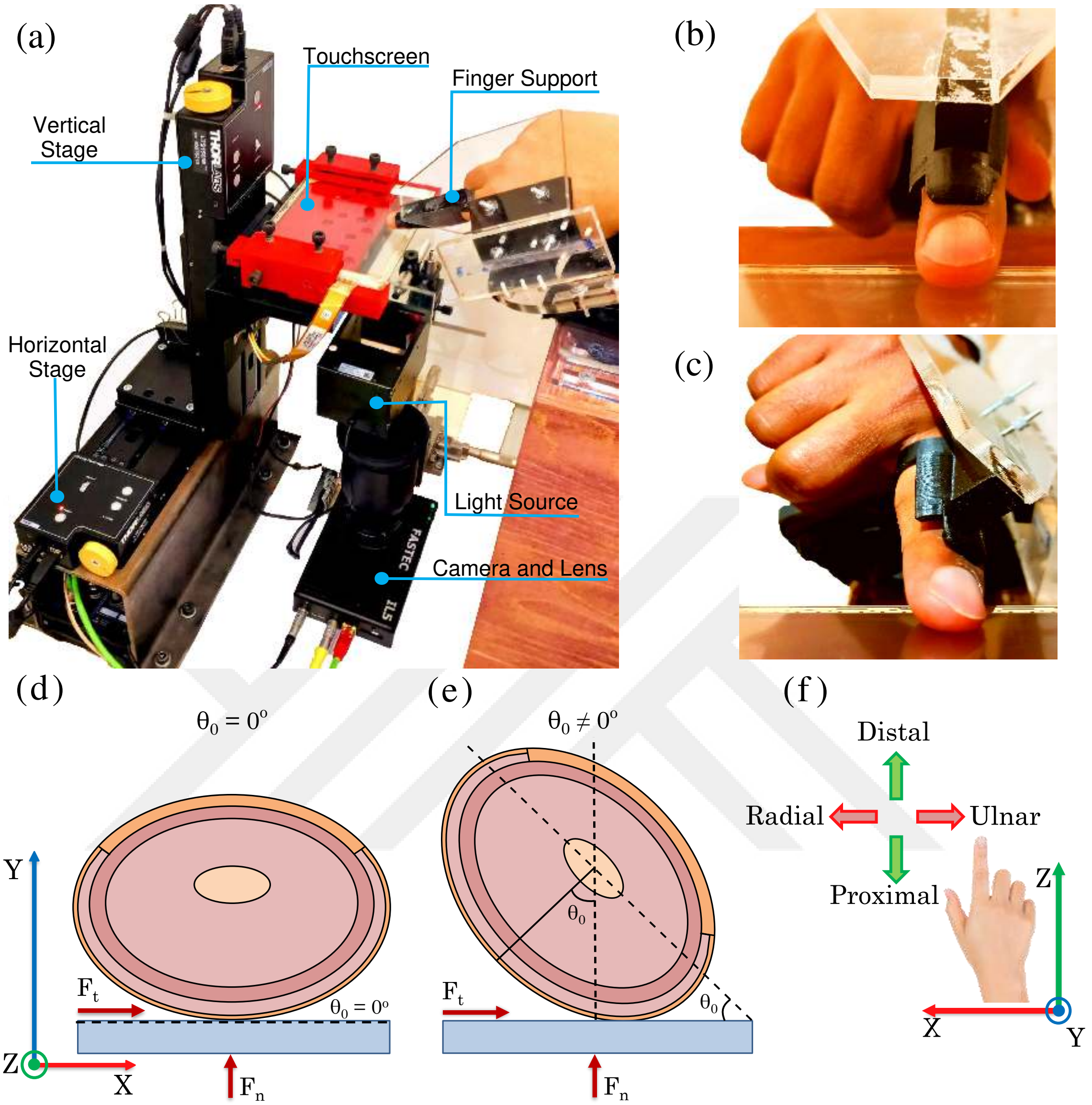

Figure 2.1: (a) The experimental setup used in our study. The index finger of each participant was fixated using the finger support at internal rotation angles of $\theta_0 = 0°$, 15°, 30°, and 45° about the longitudinal axis of the finger. The normal force and sliding velocity were controlled by vertical and horizontal stages, respectively. The contact area was illuminated by a co-axial light source and imaged by a high-speed camera. Finger configurations for (b) 0° and (c) 45° internal rotation angles. The schematic cross-sectional views of the finger for the rotation angles of (d) $\theta_0 = 0°$ and (e) $\theta_0 \neq 0°$. (f) Coordinate axes and anatomical directions used in our study.

- two linear translational stages (LTS150, Thorlabs Inc.) that enable movement of the plate in normal and tangential directions relative to the finger.
- Mini40-SI-80-4 force transducer (ATI Industrial Automation Inc.) was placed beneath the plate to measure normal and tangential forces.
- high-speed camera (IL5H, Fastec Imaging Inc.) was used to capture images of the fingerpad during the experiments.
- co-axial light source (C50C, Contrastech Inc.) was used to illuminate the contact area of the fingerpad.
- DAQ card (PCIe-6034E, National Instruments) was used to acquire the normal and tangential forces acting on the finger at a sampling frequency of 2.5 kHz.

A proportional-integral-derivative (PID) controller maintained a constant normal force on the fingerpad while sliding the plate underneath the finger in both ulnar and radial directions with a desired velocity by moving the horizontal stage. To precisely control the finger's rotation about the distal axis, custom-made hand support was fabricated via 3D printing.

The pronation of the hand (palm facing down) with respect to the plate, as shown in Figure 2.1b, was referred to as 0° rotation. The finger rotations other than the pronation position were attained by internal rotation of the right hand around its longitudinal axis (for example, Figure 2.1c illustrates 45° rotation) A custom-made hand support was manufactured by a 3D printer to control the finger's rotation precisely at desired angles. Schematic representations of the fingerpad's cross-section at rotation angles equal and not equal to zero degrees are presented in Figure 2.1d and e, respectively. The 4 anatomical directions are illustrated in Figure 2.1f.

2.2 Experiments

Our experiments comprise two parts: i) stationary finger under normal loading and ii) sliding finger under combined normal and tangential loading. The measurements were taken three times for each rotation angle. The experiments were performed with 2 male participants (S_1: 30 and S_2: 35 years old). Before the experiments, the participants washed their hands with soap and water and dried them at room temperature. The surface of the plate was cleaned carefully with ethanol. To ensure a good contrast in the captured fingerpad images, 0.5 μL of liquid vaseline was carefully applied to the participant's fingerpad using a micropipette. The participants were advised to remain stable throughout the experiments.

2.2.1 Experiments for stationary finger under normal loading

During the first experiment (stationary finger under normal loading), the plate was commanded to move 4.5 mm upwards in the normal direction with a step size of 0.1 mm. Between the steps, the plate stayed stationary for 10 seconds so that the normal force applied to the finger could reach a relaxation. We recorded the images of apparent contact area and the normal forces during the last 2 seconds of the elapsed time.

2.2.2 Experiments for sliding finger under combined normal and tangential loading

In the second experiment (sliding finger under combined normal and tangential loading), we recorded the images of the fingerpad together with the normal and tangential forces acting on the finger while the plate was slid beneath the fingerpad with a constant velocity of 20 mm/s in ulnar and radial directions under 3 normal forces (0.5, 1, and 1.5 N). Each trial started by applying a desired normal force on the fingerpad and triggering the camera to record images, followed by the horizontal motion of the plate.

2.2.3 Fingerpad's apparent contact area calculation

The apparent contact area was calculated using the approach suggested by [Delhaye et al., 2014], which involves the following three stages:

- homomorphic filtering of the raw images in which the image's pixel intensities are transformed from the spatial domain to the frequency domain and

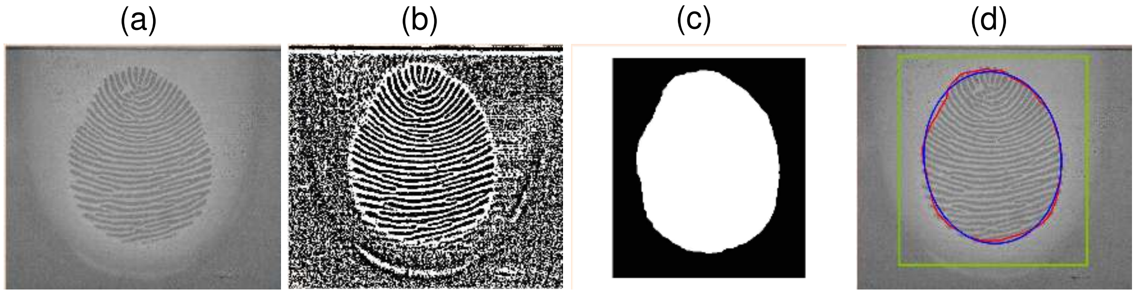

Figure 2.2: Processing of fingerpad image (a) raw image (b) output of homomorphic filtering (c) output of grey-scale mathematical morphology, and (d) green rectangle: the selected sub-region, red: contour of the elliptical area, blue: fitted ellipse.

compression of the dynamic range of pixel's intensities values making both the bright and the dark regions more balanced. A high-pass filter is applied to emphasize and suppress the high-frequency and low-frequency components, respectively, followed by inverse logarithmic transformation of the image to the spatial domain.

- identifying fingerpad contours by grey-scale mathematical morphology in which the shape of regions is altered by expanding bright areas at the expense of dark areas by "opening" (erosion followed by dilation) and "closing" (dilation followed by erosion) operations.

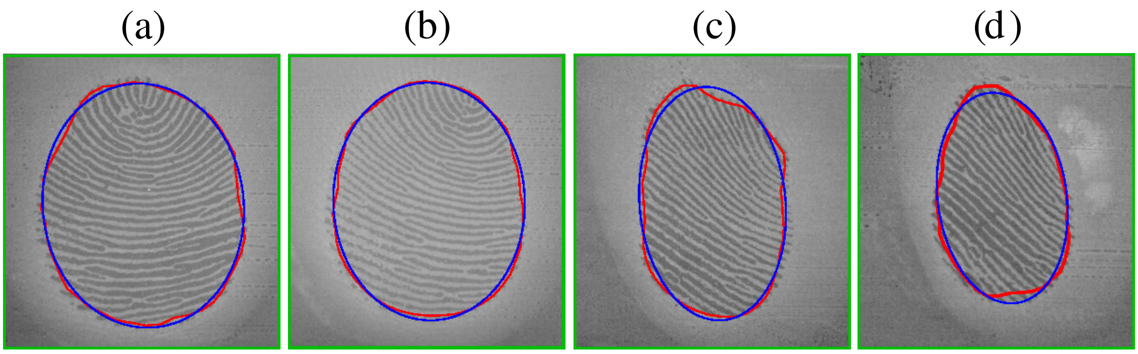

Figure 2.3: Fingerpad images of S_1 under the normal force of 1 N for the initial rotation angles of (a) $\theta_0 = 0°$, (b) $\theta_0 = 15°$, (c) $\theta_0 = 30°$, and (d) $\theta_0 = 45°$.

- Fifty equally spaced coordinates were sampled along the border of the contact area followed by fitting of the ellipse to the contact area contours.

The area of the fitted ellipse was taken as the apparent contact area of the fingerpad. Figure 2.2a-d showcases a sequence of essential visual representations, including the raw image of the fingerpad, the result of homomorphic filtering, the outcome of grey-scale mathematical morphology, and lastly, the contact area contours and its corresponding fitted ellipse respectively. Fig. 2.3a, b, c, and d depict the fingerpad contact areas of S_1 for the initial rotation angles of 0°, 15°, 30°, and 45°, respectively.

2.3 Finite element modeling (FEM)

A 2D elliptical FE model of the human fingerpad in contact with a flat plate was developed in COMSOL Multiphysics to simulate contact under pure normal loading and combined loading conditions. The model of the finger contains the nail and 4 sub-layers, including Stratum Corneum (SC), epidermis, dermis, and subcutaneous tissue attached to the bone, as shown in Figure 2.4a.

2.3.1 Material parameters and physical dimensions of FE Model

The material properties of all layers are tabulated in Table 2.1, which are adopted from the literature [Maeno et al., 1998, Fruhstorfer et al., 2000, Vodlak et al., 2016, Nam and Kuchenbecker, 2021].

The thickness of the SC, epidermis, and dermis layers are 0.1 mm, 0.6 mm, and 0.8 mm, respectively, and the major and minor radii of the 2D elliptical model are 10 mm and 7 mm, respectively. Five-parameter Mooney-Rivlin's material model was utilized for the dermis, epidermis, and subcutaneous tissue due to their hyperelastic behavior [Wu et al., 2006]. The FEM mesh comprised 21601 triangular elements (fingerpad), 800 quadrilaterals (the plate), 5541 edge elements, and 368 vertex elements. To enforce the contact constraints, the Penalty contact method was utilized. The average static and dynamic coefficients of friction (CoFs), obtained by the experiments performed in this study were incorporated into the Coulomb friction model to

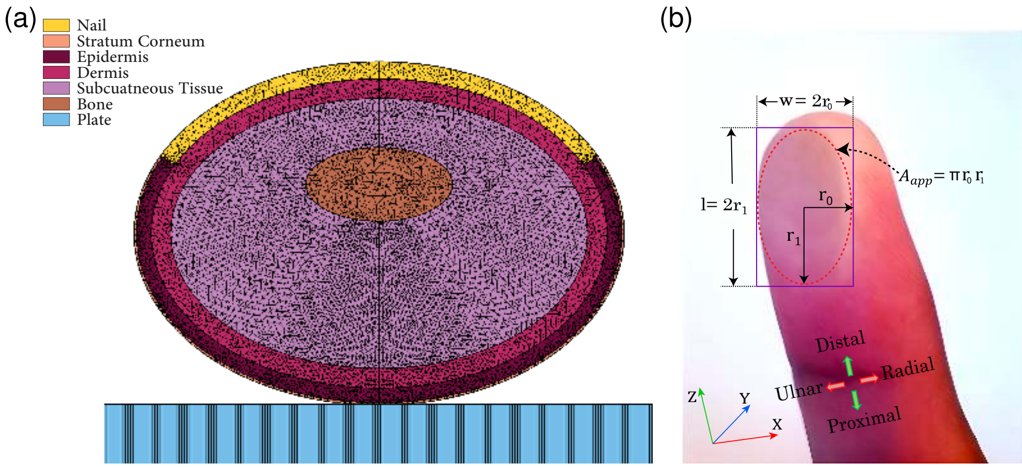

Figure 2.4: (a) 2D FEM model of the finger in contact with the plate. In this model, subcutaneous tissue, dermis, and epidermis are defined as hyperelastic materials and bone, nail, SC, and the plate are defined as elastic materials. (b) The elliptical contact area of the fingerpad ($A_{app} = \pi r_0 r_1$) was calculated by using the width of contact, $w = 2r_0$, estimated by the FEM simulations and the contact length, $l = 2r_1$, measured by the experiments.

simulate contact interactions during sliding. The mean values of force-displacement curves obtained experimentally under the normal loading condition (stationary finger) for the rotation angle of $\theta_0 = 0°$ were used to estimate the initial values of Mooney-Rivlin material constants.

The simulated elliptical fingerpad contact area, corresponding to actual elliptical contact area illustrated in Figure 2.4b, was calculated using the relation $A_{app} = \pi r_0 r_1$. In Figure 2.4b, r_0 represents half of the simulated contact width (corresponding to w in Figure 2.4b) between the SC and the plate, which varies with loading, and r_1 is half of the average fingerpad contact length ($l = 12.5mm$), which was obtained from the fingerpad images of subject S_1 under the normal force of 1 N.

2.3.2 FEM simulation procedure

The FEM simulations were performed for 4 rotation angles of the fingerpad under 2 conditions: i) normal loading (the plate was incrementally pushed upwards to

Table 2.1: **Material properties of the fingerpad layers used in the FEM model**

Layers	Hyperelastic (kPa)						Linear Elastic		
	C_{10}	C_{01}	C_{11}	C_{20}	C_{02}	(κ)	E(MPa)	ν	ρ(kg/m^3)
Subcutaneous Tissue	-59.6	64.0	-182.7	40.0	228.7	20.1	-	-	-
Dermis	-56.0	67.2	-182.7	42.5	228.7	49.4	-	-	-
Epidermis	-50.0	70.0	-182.7	48.5	228.7	92.3	-	-	-
Bone	-	-	-	-	-	-	17000	0.3	1908
Nail	-	-	-	-	-	-	17	0.3	1900
Stratum Corneum	-	-	-	-	-	-	1	0.3	1200
Plate	-	-	-	-	-	-	73100	0.3	2500

compress the finger), and ii) combined loading (the finger slid on the plate in ulnar and radial directions under a normal force of 1 N). The normal force as a function of vertical displacement (fingerpad compression) and apparent contact area as a function of normal force were recorded under the simulated normal loading condition. Apparent contact area and normal and tangential forces as a function of horizontal displacement were recorded under the simulated combined loading condition (sliding finger).

Chapter 3

RESULTS

In this chapter, the results of the experiments and finite element modeling for i) stationary finger under normal loading and ii) sliding finger under combined normal and tangential loading conditions are reported.

3.1 Experimental results

3.1.1 Results for stationary finger under normal loading

In the first experiment (stationary finger under normal loading), the images of the fingerpad, the normal force acting on the finger, and vertical displacement of the plate relative to the fingerpad were recorded in 3 separate sessions on 3 different days (4 rotation angles × 3 repetitions = 12 trials) for each subject.
Figure 3.1a and c illustrate the change in normal force as a function of the vertical displacement of the plate for S1 and S2, respectively. The normal force increases non-linearly with the vertical displacement for all rotation angles (0°, 15°, 30°, and 45°). In addition, the magnitude of normal force increases as the rotation angle is increased. Figure 3.1b and d depict the change in apparent contact area as a function of normal force for S_1 and S_2, respectively. The apparent contact area increases with normal force and nearly saturates at higher normal forces for all rotation angles. In addition, the size of the apparent contact area decreases as the rotation angle is increased.

A power-law model was fitted to the experimental data of displacement versus force and normal force versus apparent area:

$$F_n = k_F \delta^{m_F} \tag{3.1}$$

$$A^0_{app} = k_A {F_n}^{m_A} \tag{3.2}$$

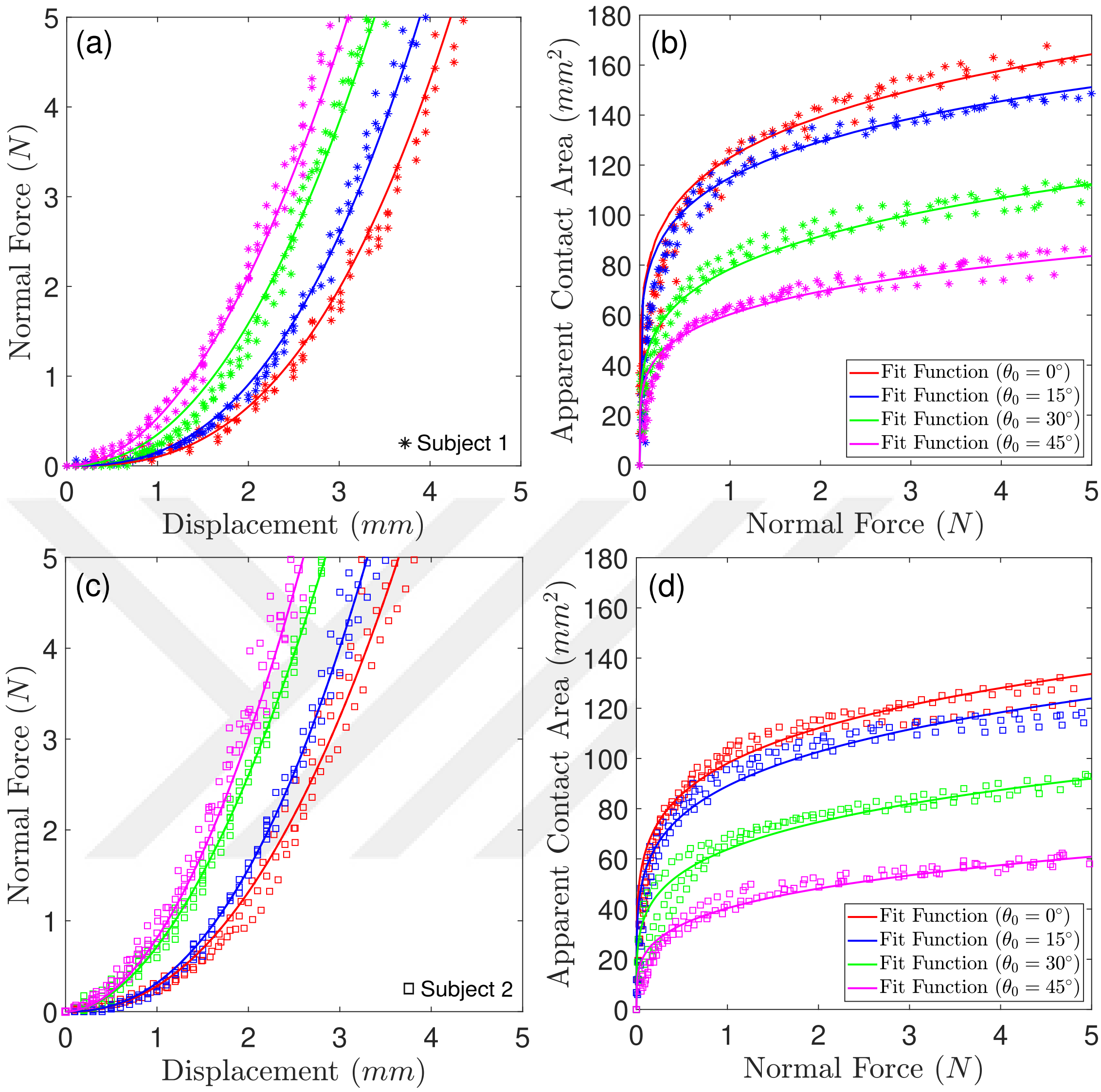

Figure 3.1: (a) Normal force acting on the fingerpad of subjects S_1 and S_2 as a function of displacement in normal loading condition. (b) The apparent contact area of subjects S_1 and S_2 as a function of normal force in normal loading condition.

where, m_i and k_i $(i = F, A)$ are the exponents and coefficients of the model, respectively. A^0_{app} is the initial apparent contact area and δ is the vertical displacement for the stationary finger (no sliding).
The results of the best-fitted curves are presented in Figure 3.1 and the values of m_i and k_i are tabulated in Table 3.1.

For both subjects, increasing the rotation angle increases the displacement coeffi-

Table 3.1: **The coefficients k_F (N/mm^{m_F}), k_A(mm^2/N^{m_A}) and exponents m_F and m_A (unitless) of the power-law models.**

Subject	Rotation Angle (degree)	k_F	m_F	R^2 ($F_n$vs.δ)	k_A	m_A	R^2(A_{app}vs.F_n)
S_1	0	0.0935	2.7300	0.99	116.3	0.1998	0.92
	15	0.1991	2.3530	0.99	106.1	0.2219	0.94
	30	0.3120	2.2750	0.99	76.82	0.2463	0.96
	45	0.5168	2.0714	0.99	56.63	0.2704	0.94
S_2	0	0.2535	2.3430	0.98	95.22	0.2158	0.93
	15	0.3280	2.2780	0.99	86.11	0.2312	0.94
	30	0.7120	1.8660	0.99	58.03	0.2637	0.66
	45	0.9504	1.7510	0.99	37.54	0.2859	0.90

cient k_F and decreases the displacement exponent m_F, whereas it decreases the load coefficient k_A and increases the load exponent m_A. It is worth noting that the values of coefficients and exponents differ for S_1 and S_2, showing the subject-dependent effects due to the differences in material properties and finger morphology such as size and shape [Derler and Gerhardt, 2012, Cornuault et al., 2015]. For example, the minor and major radii of index finger cross-section for S_1 are $6.14 \pm 0.02mm$ and $8.55 \pm 0.02mm$, and for S_2 are $5.95 \pm 0.02mm$ and $7.49 \pm 0.02mm$, respectively.

3.1.2 Results for sliding finger under combined loading

For the combined loading condition (sliding finger), the images of the fingerpad and normal and tangential forces acting on the fingerpad were acquired in 72 trials from each participant, involving 4 rotation angles, 3 normal forces, 2 sliding directions, and 3 repetitions (the experiments were performed in 3 separate sessions on 3 different days).

Figures 3.2a and b present the normalized mean values of the apparent contact area (A_{app}/A^0_{app}) and the mean values of tangential forces for the ulnar and radial sliding directions, respectively.

For the sliding in radial direction, the apparent contact area decreases for all

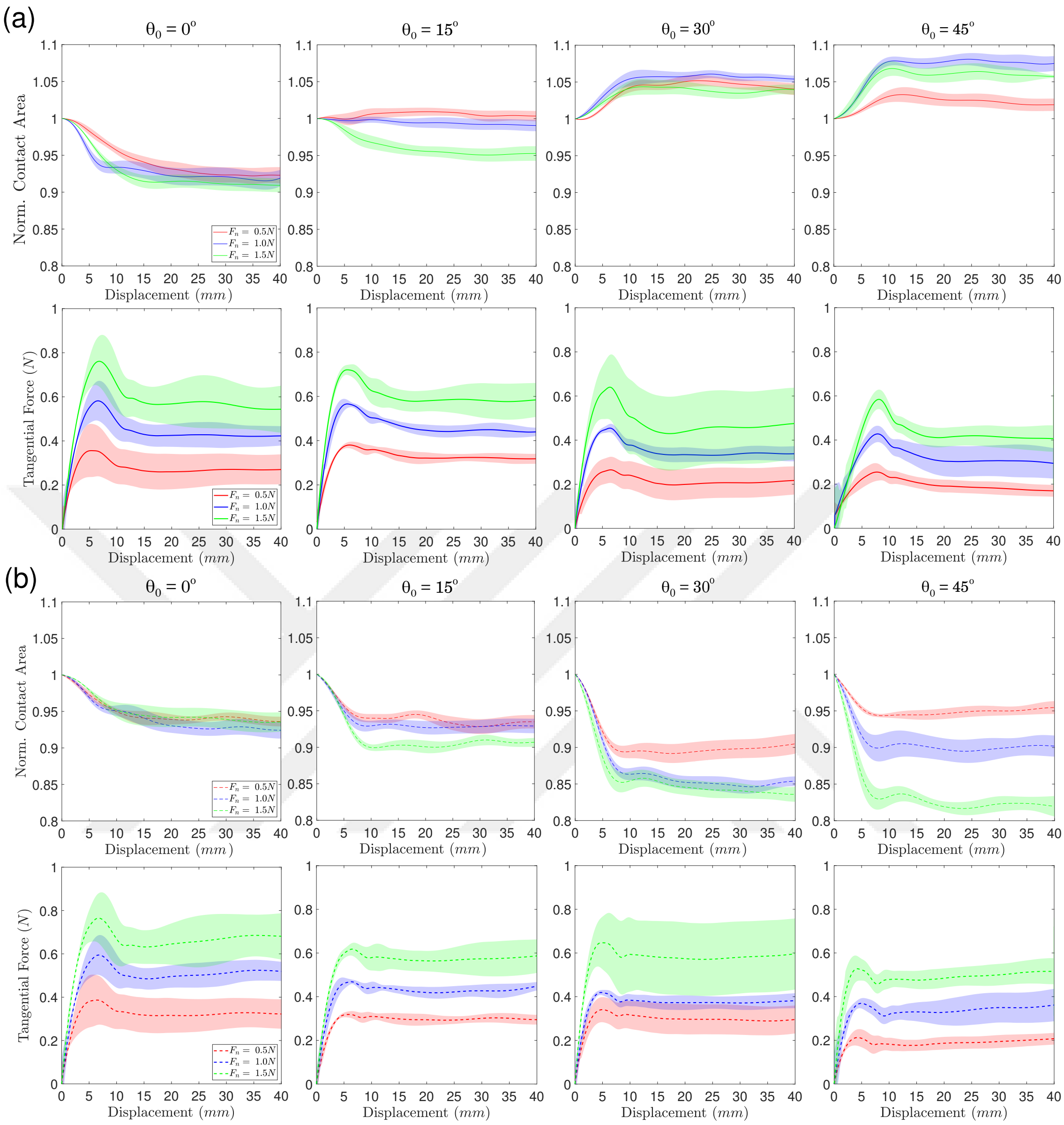

Figure 3.2: Change in normalized mean apparent contact area and mean tangential force as a function of displacement for sliding in (a) ulnar direction, and (b) radial direction for rotation angles of 0°, 15°, 30°, and 45°. Solid and dashed lines are the mean values while the shaded regions around the mean values represent the standard deviations.

rotation angles. This reduction begins at the onset of the application of tangential force and persists until the macroscopic sliding regime is attained, at which point A_{app} stabilizes around its minimum value.

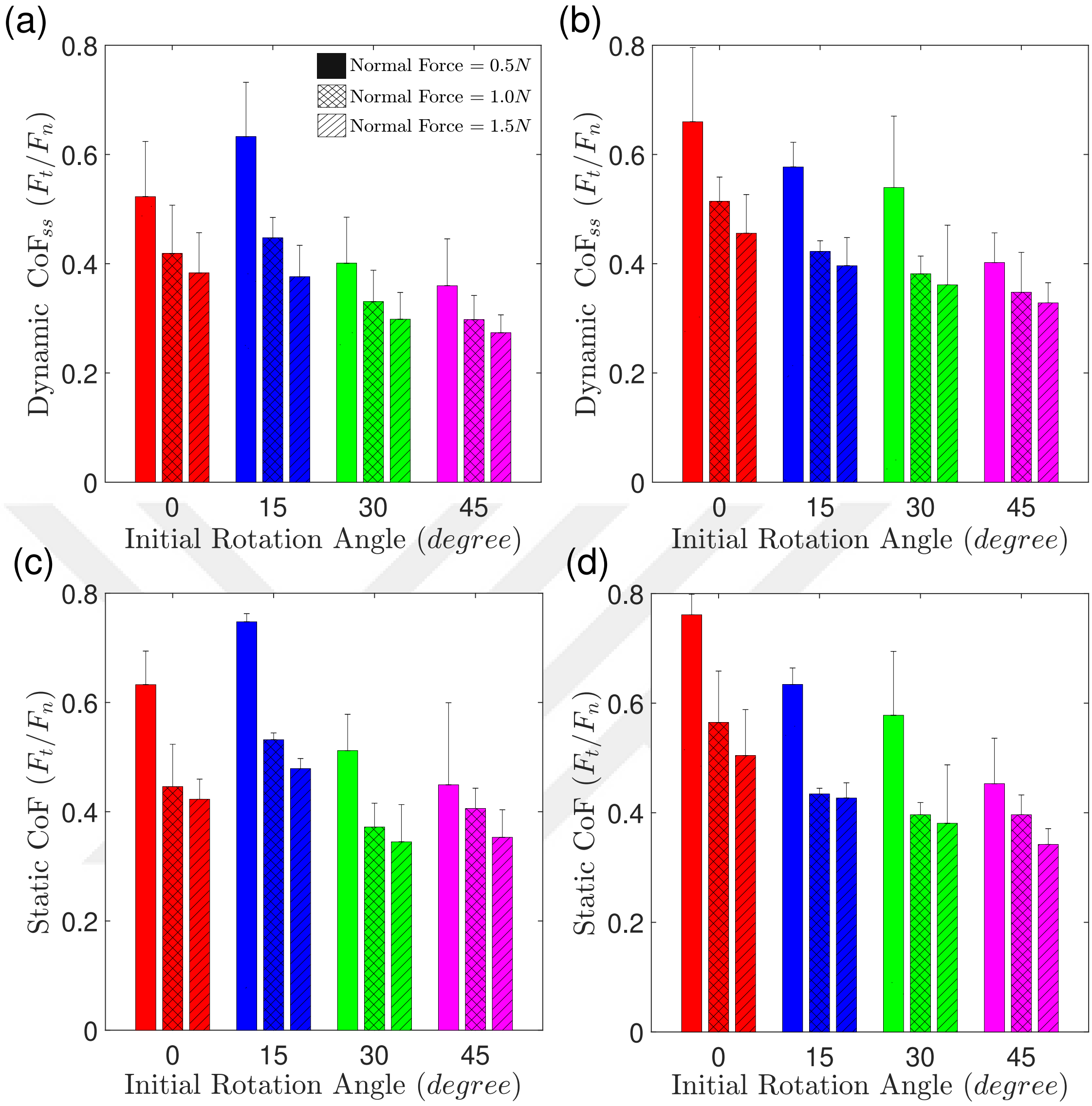

Figure 3.3: Mean values of CoF with standard deviations for 4 rotation angles under 3 different normal forces: dynamic CoF for ulnar and radial directions (a, b) and static CoF for ulnar and radial directions (c, d).

For the rotation angles of 30° and 45°, A_{app} increases for sliding in the ulnar direction under all 3 normal forces. During the ulnar sliding at 15° rotation angle, A_{app} remains almost constant under the normal forces of 0.5 N and 1 N, but a slight reduction of approximately 3% is observed for a normal force of 1.5 N. On the other hand, the results show that, regardless of the sliding direction, the static and dynamic (steady-state) CoF decreases as normal force and rotation angle increase (Figure 3.3a-d). In addition, the mean values of steady-state CoF for radial sliding were consistently higher than those for ulnar sliding for all rotation angles and normal forces except for the rotation angle of 15°.

3.2 Finite element modeling results

Figure 3.4 shows the FEM simulations of fingerpad in contact with a flat plate under normal loading and combined loading conditions for 0° (first row), 30° internal rotation (second row), and 30° external rotation (third row) of the finger. To replicate the normal loading condition, the plate was moved in the vertical direction and incrementally compressed the stationary finger.

In the sliding condition (combined loading), first a normal force of 1 N was applied and maintained by regulating the vertical movement of the plate against the stationary finger for 30 seconds. Subsequently, the plate was slid in ulnar/radial direction, inducing tangential traction on the fingerpad as a result of friction between the fingerpad and the plate. The mean CoFs obtained experimentally at different rotation angles (Figure 3.3a-d) were utilized in the corresponding simulations. The images in Figure 3.4a show Von Mises stress distribution across the cross-section of fingerpad for initial contact, normal loading, and combined loading for sliding in ulnar and radial directions.

Figure 3.4b and c illustrate the change in apparent area as a function of displacement between 30° internal and external rotations during sliding in the ulnar and radial directions, respectively. Notably, for both ulnar and radial directions, the change in apparent area during internal rotation exhibits an opposite trend to that observed during external rotation of the finger.

The results of normal force as a function of vertical displacement (compression of the fingerpad by the plate) and the change apparent contact area as a function of normal force for 4 rotation angles are presented in Figure 3.5a and b, respectively. The trends observed in FEM simulations match well with those of the experimental results reported in Figure 3.1.

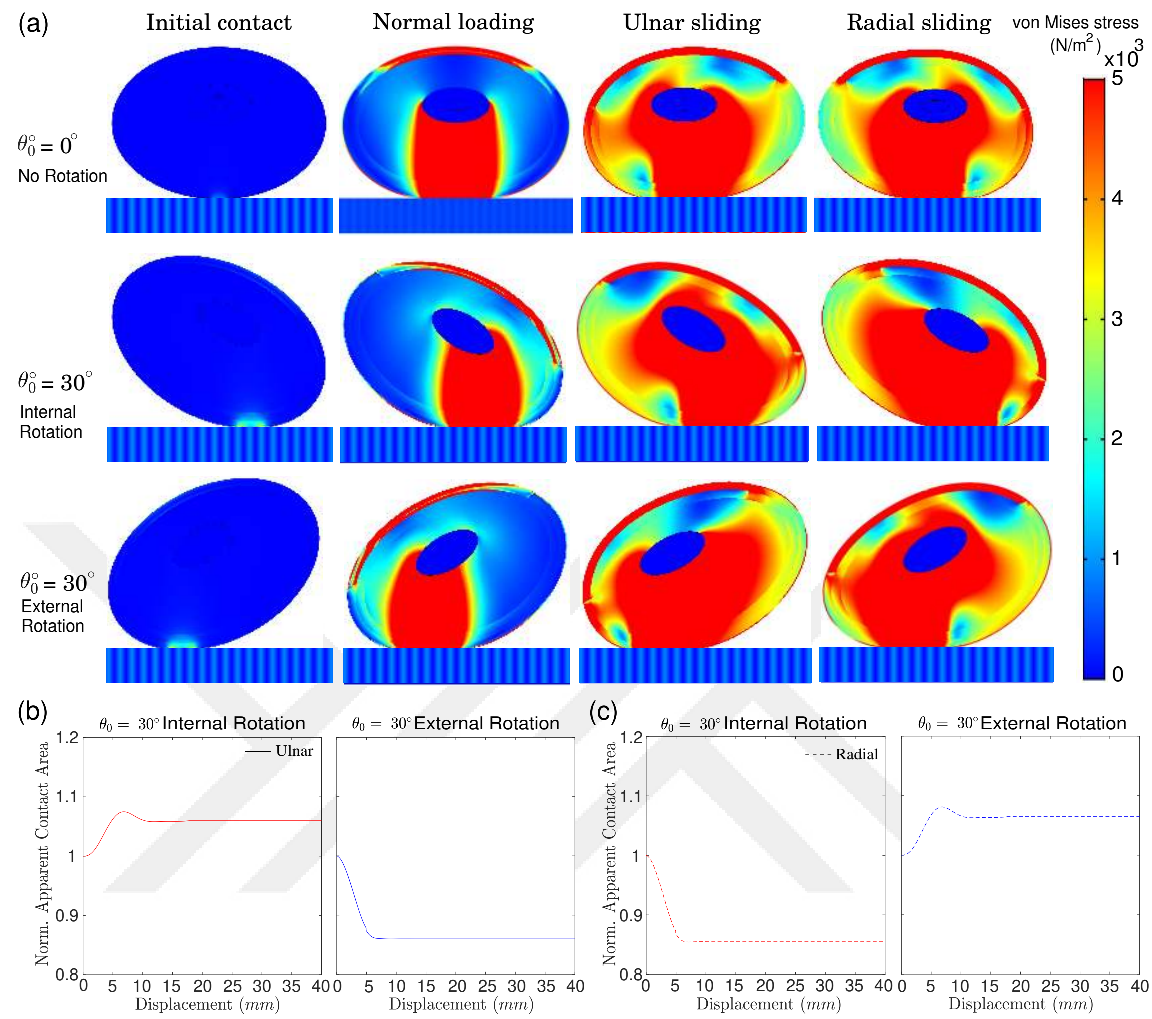

Figure 3.4: (a) FEM simulations of the fingerpad under normal and combined loading conditions for the rotation angles of 0° (first row), 30° internal rotation (pronation, second row), and 30° external rotation (supination, third row). A normal force of 1 N was applied and maintained for 30 seconds followed by horizontal sliding of the finger. The images present Von Mises stress distribution across the fingerpad for initial contact, normal loading, and combined loading for sliding in ulnar and radial directions. (b) Comparison of change in apparent area as a function of displacement in ulnar and radial directions for 30° internal rotation to 30° external rotation.

The simulation results for the apparent contact area under the sliding condition are presented in Figure 3.5c, which are inline with the experimental results reported in Figure 3.2. For the rotation angle of 0°, the apparent contact area, A_{app}, shrinks

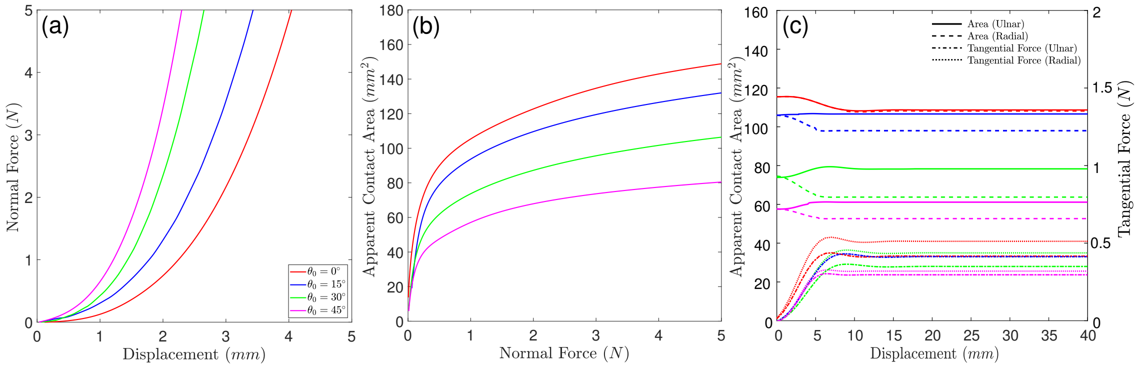

Figure 3.5: Results of the FEM simulations. (a) Change in normal force as a function of plate displacement and (b) change in apparent contact area as a function of the normal force under normal loading condition. (c) Change in apparent contact area as a function of sliding displacement for 4 orientations of the fingerpad under combined loading condition. A normal force of 1 N was applied and maintained for 30 seconds followed by horizontal sliding of the finger.

and eventually reaches a steady-state value during sliding in ulnar and radial directions. However, A_{app} increases during the ulnar sliding while it still decreases during the radial sliding for the rotation angles of 30° and 45°, as observed in the experiments. For the rotation angle of 15°, A_{app} remains almost constant during the ulnar sliding and decreases during the radial sliding with trends similar to the corresponding experimental results.

Chapter 4

DISCUSSION

The main focus of this study was to examine how the initial rotation of the finger about its distal axis affects the evolution of the apparent contact area. The experimental investigation was carried out under two conditions: pure normal loading with a stationary finger, and combined normal and tangential loading while the plate was slid beneath the fingerpad in the ulnar and radial directions.

4.1 Apparent contact area evolution under normal loading

The change in normal force as a function of displacement under normal loading was modeled by a power-law function (Eq. (3.1)), but the displacement exponents (m_F) estimated from the experimental data for 4 rotation angles are different from the Hertzian displacement exponent of 3/2, as also observed in the earlier studies [Tomlinson et al., 2011].

Similarly, the load exponents (m_A) estimated from the experimental data of normal force versus apparent contact area for 4 rotation angles also differ from the Hertzian load exponent of 2/3 [Huloux et al., 2021]. We observed that, under normal loading, the apparent contact area is reduced and the finger becomes stiffer as the rotation angle is increased (Figure 3.1). This suggests that there are greater geometric constraints closer to the radial edge compared to the palmar edge.

Even though the experimental data shows that the contact behavior is non-Hertzian, this stiffening behavior can be better visualized if the effective elastic modulus, E^*, is calculated based on the Hertz model using the following equation:

$$E^* = \frac{3F_n}{4\delta}\left[\frac{\pi}{A^0_{app}}\right]^{1/2} \tag{4.1}$$

Equation (4.1) was utilized to calculate the effective elastic modulus of the fingerpad

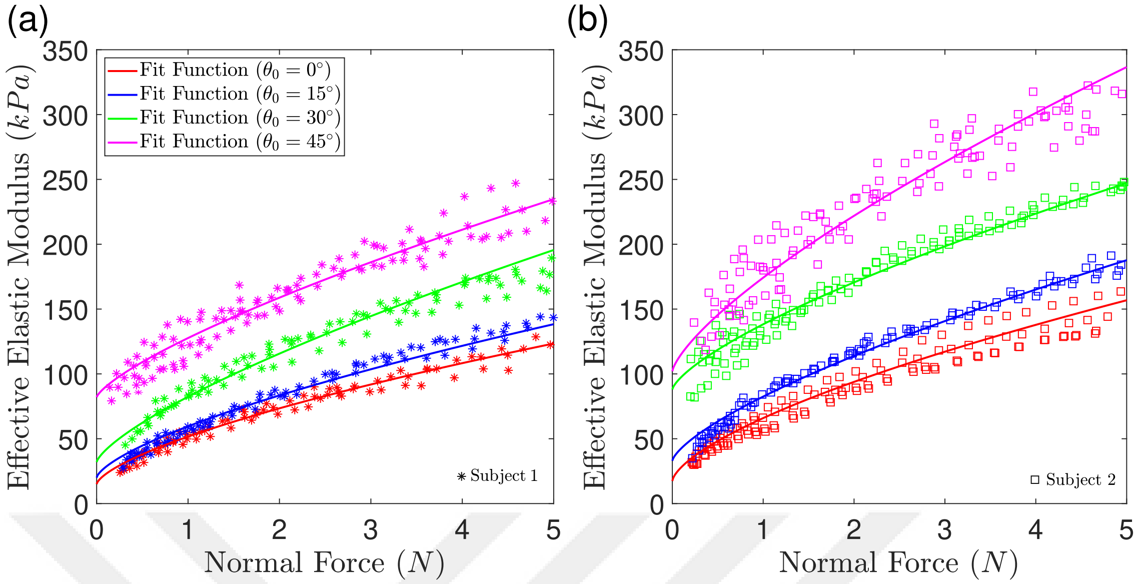

Figure 4.1: Effective elastic modulus of the fingerpad as a function of normal force based on the experimental data collected under normal loading condition (a) for S_1 and (b) for S_2.

as a function of normal force using the experimental data collected for the normal loading condition. Table 4.1 tabulates the coefficients (E_0 and β) and exponent (γ) estimated from the experimental data by fitting a power-law model of $E^* = E_0 + \beta F_n^\gamma$. The results presented in Figure 4.1 show an increase in the effective elastic modulus of the fingerpad as a function of normal force, while the increase in elastic modulus as a function of rotation angle appears to be nonlinear. [Dzidek et al., 2017] and [Oprişan et al., 2016] also reported a similar linear relation between the secant modulus and normal force for the contacts between fingerpad and a smooth surface. They argued that the secant modulus approaches Young's modulus as F_n approaches zero. Moreover, across all experimental conditions, the effective elastic modulus values of S_1 are consistently lower than that of S_2. This discrepancy is attributed to higher apparent contact areas for S_1 compared to S_2 in addition to other influencing factors, such as age, gender, and environmental conditions [Derler and Gerhardt, 2012]. The similar dependency of effective elastic modulus on the length scale of the contact has been reported in the literature [Van Kuilenburg et al., 2013]. Our results show that the elastic modulus of the fingerpad changes with finger rotation about its axial axis, which impels us to consider its effect in developing analytical models interpreting the evolution of apparent contact area as a function of normal force.

Table 4.1: **Initial elastic modulus, E_0 (kPa), coefficient of normal force β (kN$^{(1-\gamma)}$/m^2), and normal force exponent γ (unitless) shown in Figure 4.1.**

Subject	Rotation Angle (degree)	E_0	β	γ	R^2
S_1	0	15	36.64	0.674	0.94
	15	20	39.55	0.681	0.96
	30	32	50.36	0.732	0.91
	45	82	45.64	0.751	0.93
S_2	0	25	41.26	0.635	0.98
	15	33	52.74	0.657	0.96
	30	88	53.21	0.676	0.83
	45	102	87.75	0.732	0.84

4.2 Apparent contact area evolution under combined normal and tangential loading

The latter part of this study focused on the anisotropic change in the apparent contact area of the fingerpad during sliding in ulnar and radial directions for 4 different axial rotations of the finger relative to the plate. For the rotation angle of 0°, reduction in A_{app} starts at the onset of sliding in both ulnar and radial directions. The reduction in the apparent area as a function of displacement observed in our experiments for 0° rotation angle (Figure 3.2a) is similar to those observed in the earlier experimental studies [Delhaye et al., 2014, Sahli et al., 2018, Sirin et al., 2019].

The reduction in apparent area is roughly equal for the ulnar (7.8%) and radial (7.3%) sliding directions in our experiments. This similarity can be attributed to the symmetry in the finger geometry and contact loading at 0° rotation angle. For example, the radius of curvature changes symmetrically while moving from the palmar edge to either the radial or the distal edge of the fingerpad.

[Sahli et al., 2018] proposed an empirical relation ($A_{app} = A^{o}_{app} - \alpha F_t^2$) for the shear-induced reduction in area as a function of tangential force observed during the sliding of a soft sphere on a rigid plate, in which the contact region evolves from a circular area under pure normal load to a reduced elliptical area in the macroscopic sliding regime. Where the parameter α is independent of tangential force (F_t) but dependent on the normal load (F_n) and the initial contact area (A^{o}_{app}). [Papangelo et al., 2019] concluded that the reduction in contact area doesn't solely follow a linear decrease with F_t^2, but rather exhibits a relationship with an exponent η, which is also influenced by the normal load. Moreover, the original form of this relation loses its applicability to sliding contact between an initially rotated fingerpad and a plate because of the changes in the radius of curvature and asymmetries in contact loading, as observed in our study.

Non-linear stiffening of the fingerpad's skin and its finite deformations, which induce strong coupling between normal and tangential effects, have been reported among the causes behind the shear-induced area reduction [Delhaye et al., 2014, Babu et al., 2018, Lengiewicz et al., 2020]. In particular, contact lifting at the trailing edge was reported to contribute 90-95% to the total area reduction in [Lengiewicz et al., 2020]. Through FEM simulations of the sliding finger under electroadhesion, [Forsbach et al., 2023] reported a 12% reduction in contact length. They showed that the increased tangential loading due to electroadhesion results in a torsional motion of the tissue around the fingertip's fixed bone, causing the ridges at the trailing edge to lift while new ridges contact the surface at the leading edge. The contact area changes described in [Forsbach et al., 2023] are similar to those in the combined loading condition in our study. However, our FEM model did not include finger ridges, preventing the observation of staircase-like variations in contact area. Similarly, du Bois de Dunilac et al. [du Bois de Dunilac et al., 2023] also reported a $15 \pm 11\%$ reduction in the apparent contact area of fingerpad under torsional loading about the palmar axis. They argued that the reduction was mainly driven

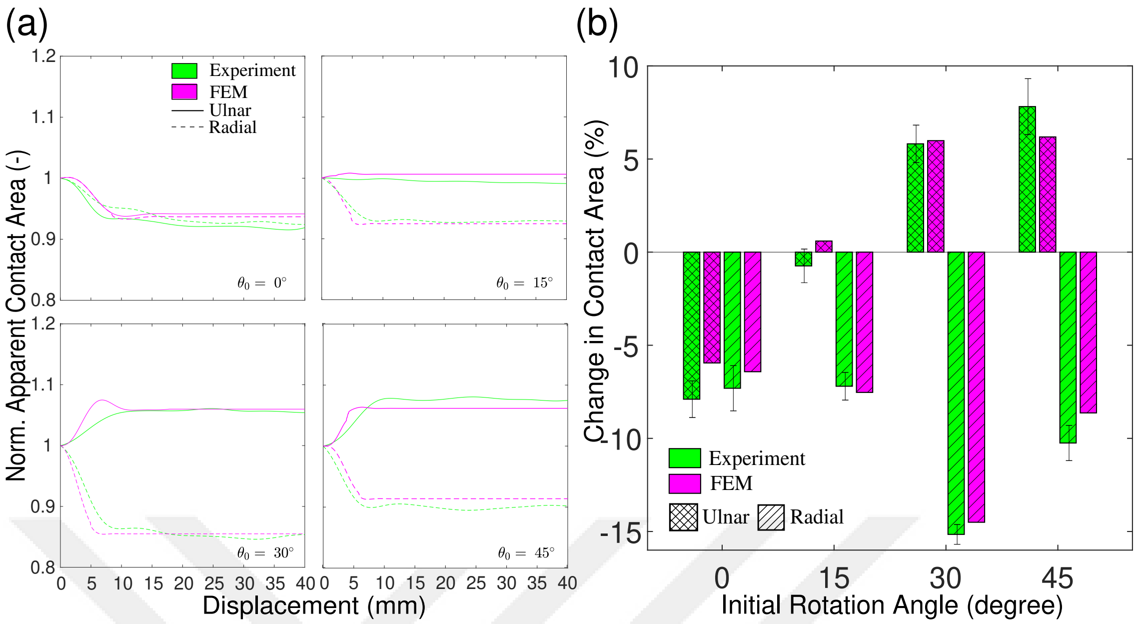

Figure 4.2: Comparison between experimental and FEM results. The curves depicting the experimental data are derived from the average of two subjects. (a) Normalized apparent contact area as a function of displacement for ulnar and radial directions and (b) percentage change in contact area, with corresponding standard deviations for experimental results, as a function of the rotation angles for sliding in ulnar and radial directions.

by two mechanisms: peeling, where the fingerpad skin loses contact with the plate, and deformation, due to in-plane skin compression, measured by computer vision techniques. Peeling was identified as the dominant factor contributing to the area change in their study.

In our study, the amount of reduction in contact area was influenced by the rotation angle during radial sliding and the relation between them was not linear. Our experimental results for the radial direction were supported by the FEM simulations (see the comparisons in Figure 4.2a). A reduction of 7.3%, 7.2%, 15.1%, and 10.2% was observed in apparent area at 0°, 15°, 30°, and 45° rotation angles, respectively (Figure 4.2b). On the other hand, during ulnar sliding, the change in contact area progressively shifted from a decrease at 0° (7.8% reduction) to a negligible amount (0.7% reduction) at 15° , followed by an increase of 5.8% and 7.8%

at the rotation angles of 30° and 45°, respectively (Figure 4.2b). The experimental results on ulnar direction are also supported by the FEM simulations (Figure 4.2b). The increase in the apparent contact area at the rotation angles of 30° and 45° is surprising and has not been reported in the literature before. As suggested in [Delhaye et al., 2014, Lengiewicz et al., 2020], the stiffening of the fingerpad appears to play a role in area change since Figure 4.1 shows that the effective elastic modulus of fingerpad increases non-linearly as the rotation angle is increased. The stiffening and relaxation of the fingerpad skin in varying degrees in response to the respective increase and decrease in the tangential forces cause a change in apparent contact area and non-uniform stress distribution at the contact as analyzed by computer vision techniques in [Delhaye et al., 2016, Ozdamar et al., 2020].

We argue that the initial finger rotation around its distal axis introduces contact asymmetries due to changes in the radius of curvature and effective elastic modulus. These asymmetries influence the contact area under both normal and combined loading conditions. With an initial rotation of 30° and 45°, the index finger rotates further toward the middle finger during the onset of ulnar sliding, thereby increasing the radius of curvature and consequently increasing the apparent contact area. Additionally, variations in effective elastic modulus from radial to palmar edge create asymmetric stress distribution at the fingerpad's leading and trailing edges, as shown in our FEM simulations (see Fig. 3.4), contributing to anisotropic changes in the contact area. These findings highlight the importance of accounting for changes in the finger's contact area during rotation when designing tactile displays and robotic hands to better mimic human hand physiology.

Moreover, "in-plane deformation" resulting from in-plane compression and dilation, "contact laying" at the leading edge, and "contact lifting" or "peeling" at the trailing edge are reported as the mechanisms involved in area reduction in the case of a spherical elastomer sliding over a smooth glass plate. In particular, "contact lifting" at the trailing edge contributes 90-95% to the total area reduction, "in-plane deformation" contributes 5-10%, and "contact laying" at the leading edge contributes nearly 0% [Lengiewicz et al., 2020].

Chapter 5

CONCLUSION

5.1 Conclusion

Investigating the contact mechanics between the human fingerpad and a smooth surface during sliding is an open area of research. In this study, we performed experiments to investigate the rotation-dependent evolution of the contact area between the index finger and a smooth flat surface under normal loading (stationary finger) and combined loading (sliding finger) conditions. The experimental results were validated by FEM simulations. The experimental and FEM results support each other and show a reduction in the apparent contact area for the radial sliding direction while a surprising increase for the ulnar direction at higher rotation angles. This result suggests that the changes in contact geometry (due to change in equivalent radius of curvature with rotation of the finger) and material properties (due to stiffening of the fingerpad as the rotation angle increases) cause an asymmetric change in contact area for the radial and ulnar directions. The findings of this study help to improve our understanding of how we touch, explore, and manipulate objects around us in our daily lives.

In our current study, the change in equivalent radius of curvature and material properties due to the rotation of finger were coupled due to its morphological structure. In the future, we plan to mold spherical and ellipsoidal elastomer samples having different material properties to investigate their distinct contribution to the anisotropic change in contact area which, we believe, will further improve our understanding of the contact mechanics between human fingerpad and a smooth flat surface.

BIBLIOGRAPHY

[Adams et al., 2007] Adams, M. J., Briscoe, B. J., and Johnson, S. A. (2007). Friction and lubrication of human skin. *Tribology Letters*, 26:239–253.

[Adams et al., 2013] Adams, M. J., Johnson, S. A., Lefèvre, P., Lévesque, V., Hayward, V., André, T., and Thonnard, J.-L. (2013). Finger pad friction and its role in grip and touch. *Journal of The Royal Society Interface*, 10(80):20120467.

[AliAbbasi et al., 2022] AliAbbasi, E., Sormoli, M. A., and Basdogan, C. (2022). Frequency-dependent behavior of electrostatic forces between human finger and touch screen under electroadhesion. *IEEE Transactions on Haptics*, 15(2):416–428.

[Babin and Gosselin, 2021] Babin, V. and Gosselin, C. (2021). Mechanisms for robotic grasping and manipulation. *Annual Review of Control, Robotics, and Autonomous Systems*, 4:573–593.

[Babu et al., 2018] Babu, D., Konyo, M., Nagano, H., and Tadokoro, S. (2018). Introducing whole finger effects in surface haptics: An extended stick-slip model incorporating finger stiffness. *IEEE Transactions on Haptics*, 11(3):417–430.

[Basdogan et al., 2020] Basdogan, C., Sormoli, M. R. A., and Sirin, O. (2020). Modeling sliding friction between human finger and touchscreen under electroadhesion. *IEEE Transactions on Haptics*, 13(3):511–521.

[Bowden and Tabor, 1964] Bowden, F. P. and Tabor, D. (1964). *The Friction and Lubrication of Solids-Part II.* Oxford, England, University Press.

[Burstedt et al., 1997a] Burstedt, M., Edin, B. B., and Johansson, R. S. (1997a). Coordination of fingertip forces during human manipulation can emerge from independent neural networks controlling each engaged digit. *Experimental Brain Research*, 117(1):67–79.

[Burstedt et al., 1997b] Burstedt, M. K., Birznieks, I., Edin, B. B., and Johansson, R. S. (1997b). Control of forces applied by individual fingers engaged in restraint of an active object. *Journal of Neurophysiology*, 78(1):117–128.

[Corniani et al., 2022] Corniani, G., Casal, M. A., Panzeri, S., and Saal, H. P. (2022). Population coding strategies in human tactile afferents. *PLOS Computational Biology*, 18(12):e1010763.

[Cornuault et al., 2015] Cornuault, P.-H., Carpentier, L., Bueno, M.-A., Cote, J.-M., and Monteil, G. (2015). Influence of physico-chemical, mechanical and morphological fingerpad properties on the frictional distinction of sticky/slippery surfaces. *Journal of The Royal Society Interface*, 12(110):20150495.

[Delhaye et al., 2016] Delhaye, B., Barrea, A., Edin, B. B., Lefevre, P., and Thonnard, J.-L. (2016). Surface strain measurements of fingertip skin under shearing. *Journal of The Royal Society Interface*, 13(115):20150874.

[Delhaye et al., 2014] Delhaye, B., Lefevre, P., and Thonnard, J.-L. (2014). Dynamics of fingertip contact during the onset of tangential slip. *Journal of The Royal Society Interface*, 11(100):20140698.

[Derjaguin et al., 1975] Derjaguin, B. V., Muller, V. M., and Toporov, Y. P. (1975). Effect of contact deformations on the adhesion of particles. *Journal of Colloid and Interface Science*, 53(2):314–326.

[Derler and Gerhardt, 2012] Derler, S. and Gerhardt, L.-C. (2012). Tribology of skin: review and analysis of experimental results for the friction coefficient of human skin. *Tribology Letters*, 45(1):1–27.

[Derler et al., 2009] Derler, S., Gerhardt, L.-C., Lenz, A., Bertaux, E., and Hadad,

M. (2009). Friction of human skin against smooth and rough glass as a function of the contact pressure. *Tribology International*, 42(11-12):1565–1574.

[du Bois de Dunilac et al., 2023] du Bois de Dunilac, S., Córdova Bulens, D., Lefèvre, P., Redmond, S. J., and Delhaye, B. P. (2023). Biomechanics of the finger pad in response to torsion. *Journal of the Royal Society Interface*, 20(201):20220809.

[Dzidek et al., 2017] Dzidek, B. M., Adams, M. J., Andrews, J. W., Zhang, Z., and Johnson, S. A. (2017). Contact mechanics of the human finger pad under compressive loads. *Journal of The Royal Society Interface*, 14(127):20160935.

[Fawcett, 1986] Fawcett, D. (1986). Hypophysis. *A textbook of histology, 11th Ed. Philadelphia, WB Saunders Co*, pages 479–499.

[Forsbach et al., 2023] Forsbach, F., Heß, M., and Papangelo, A. (2023). A two-scale fem-bam approach for fingerpad friction under electroadhesion. *Frontiers in Mechanical Engineering*, 8:1074393.

[Fruhstorfer et al., 2000] Fruhstorfer, H., Abel, U., Garthe, C.-D., and Knüttel, A. (2000). Thickness of the stratum corneum of the volar fingertips. *Clinical Anatomy: The Official Journal of the American Association of Clinical Anatomists and the British Association of Clinical Anatomists*, 13(6):429–433.

[Gray, 1878] Gray, H. (1878). *Anatomy of the human body*, volume 8. Lea & Febiger.

[Greenwood and Williamson, 1966] Greenwood, J. A. and Williamson, J. P. (1966). Contact of nominally flat surfaces. *Proceedings of the Royal Society of London. Series A. Mathematical and Physical Sciences*, 295(1442):300–319.

[Huloux et al., 2021] Huloux, N., Willemet, L., and Wiertlewski, M. (2021). How to measure the area of real contact of skin on glass. *IEEE Transactions on Haptics*, 14(2):235–241.

[Hutchinson et al., 1990] Hutchinson, J. W. et al. (1990). Mixed mode fracture mechanics of interfaces. *Metal-ceramic interfaces*, 1990:295–306.

[Jacobs and Martini, 2017] Jacobs, T. D. and Martini, A. (2017). Measuring and understanding contact area at the nanoscale: a review. *Applied Mechanics Reviews*, 69(6):060802.

[Johnson et al., 1971] Johnson, K. L., Kendall, K., and Roberts, a. (1971). Surface energy and the contact of elastic solids. *Proceedings of the Royal Society of London. A. Mathematical and Physical Sciences*, 324(1558):301–313.

[Kishishita et al., 2021] Kishishita, K., Sakamoto, N., Muranami, H., Hattori, K., and Kurita, Y. (2021). Effect of surface textures on the fingertip forces perception and output. In *2021 IEEE World Haptics Conference (WHC)*, pages 25–30. IEEE.

[Lengiewicz et al., 2020] Lengiewicz, J., de Souza, M., Lahmar, M. A., Courbon, C., Dalmas, D., Stupkiewicz, S., and Scheibert, J. (2020). Finite deformations govern the anisotropic shear-induced area reduction of soft elastic contacts. *Journal of the Mechanics and Physics of Solids*, 143:104056.

[Maegawa et al., 2015] Maegawa, S., Itoigawa, F., and Nakamura, T. (2015). Effect of normal load on friction coefficient for sliding contact between rough rubber surface and rigid smooth plane. *Tribology International*, 92:335–343.

[Maeno et al., 1998] Maeno, T., Kobayashi, K., and Yamazaki, N. (1998). Relationship between the structure of human finger tissue and the location of tactile receptors. *JSME International Journal Series C Mechanical Systems, Machine Elements and Manufacturing*, 41(1):94–100.

[Mergel et al., 2019] Mergel, J. C., Sahli, R., Scheibert, J., and Sauer, R. A. (2019). Continuum contact models for coupled adhesion and friction. *The Journal of Adhesion*, 95(12):1101–1133.

[Mergel et al., 2021] Mergel, J. C., Scheibert, J., and Sauer, R. A. (2021). Contact with coupled adhesion and friction: Computational framework, applications, and new insights. *Journal of the Mechanics and Physics of Solids*, 146:104194.

[Nam and Kuchenbecker, 2021] Nam, S. and Kuchenbecker, K. J. (2021). Optimizing a viscoelastic finite element model to represent the dry, natural, and moist human finger pressing on glass. *IEEE Transactions on Haptics*, 14(2):303–309.

[Nosonovsky and Bhushan, 2007] Nosonovsky, M. and Bhushan, B. (2007). Multiscale friction mechanisms and hierarchical surfaces in nano-and bio-tribology. *Materials Science and Engineering: R: Reports*, 58(3-5):162–193.

[Oprişan et al., 2016] Oprişan, C., Cârlescu, V., Barnea, A., Prisacaru, G., Olaru, D., and Plesu, G. (2016). Experimental determination of the young's modulus for the fingers with application in prehension systems for small cylindrical objects. In *IOP Conference Series: Materials Science and Engineering*, volume 147, page 012058. IOP Publishing.

[Ozdamar et al., 2020] Ozdamar, I., Alipour, M. R., Delhaye, B. P., Lefevre, P., and Basdogan, C. (2020). Step-change in friction under electrovibration. *IEEE Transactions on Haptics*, 13(1):137–143.

[Papangelo et al., 2019] Papangelo, A., Scheibert, J., Sahli, R., Pallares, G., and Ciavarella, M. (2019). Shear-induced contact area anisotropy explained by a fracture mechanics model. *Physical Review E*, 99(5):053005.

[Pasumarty et al., 2011] Pasumarty, S. M., Johnson, S. A., Watson, S. A., and Adams, M. J. (2011). Friction of the human finger pad: influence of moisture, occlusion and velocity. *Tribology Letters*, 44:117–137.

[Persson et al., 2013] Persson, B., Kovalev, A., and Gorb, S. (2013). Contact mechanics and friction on dry and wet human skin. *Tribology Letters*, 50(1):17–30.

[Persson, 2001] Persson, B. N. (2001). Theory of rubber friction and contact mechanics. *The Journal of Chemical Physics*, 115(8):3840–3861.

[Persson, 2006] Persson, B. N. (2006). Contact mechanics for randomly rough surfaces. *Surface Science Reports*, 61(4):201–227.

[Rubin et al., 1998] Rubin, M., Bodner, S., and Binur, N. (1998). An elastic–viscoplastic model for excised facial tissues.

[Sahli et al., 2018] Sahli, R., Pallares, G., Ducottet, C., Ali, I. B., Al Akhrass, S., Guibert, M., and Scheibert, J. (2018). Evolution of real contact area under shear and the value of static friction of soft materials. *Proceedings of the National Academy of Sciences*, 115(3):471–476.

[Sahli et al., 2019] Sahli, R., Pallares, G., Papangelo, A., Ciavarella, M., Ducottet, C., Ponthus, N., and Scheibert, J. (2019). Shear-induced anisotropy in rough elastomer contact. *Physical Review Letters*, 122(21):214301.

[Savkoor and Briggs, 1977] Savkoor, A. and Briggs, G. (1977). The effect of tangential force on the contact of elastic solids in adhesion. *Proceedings of the Royal Society of London. A. Mathematical and Physical Sciences*, 356(1684):103–114.

[Scheibert et al., 2020] Scheibert, J., Sahli, R., and Peyrard, M. (2020). Onset of sliding of elastomer multicontacts: Failure of a model of independent asperities to match experiments. *Frontiers in Mechanical Engineering*, 6:18.

[Serhat et al., 2022] Serhat, G., Vardar, Y., and Kuchenbecker, K. J. (2022). Contact evolution of dry and hydrated fingertips at initial touch. *PLoS ONE*, 17(7):e0269722.

[Sirin et al., 2019] Sirin, O., Barrea, A., Lefèvre, P., Thonnard, J.-L., and Basdogan, C. (2019). Fingerpad contact evolution under electrovibration. *Journal of the Royal Society Interface*, 16(156):20190166.

[Somer et al., 2015] Somer, D., Perić, D., de Souza Neto, E., and Dettmer, W. (2015). A multi-scale computational assessment of channel gating assumptions within the meissner corpuscle. *Journal of Biomechanics*, 48(1):73–80.

[Tabor, 1977] Tabor, D. (1977). Surface forces and surface interactions. In *Plenary and invited lectures*, pages 3–14. Elsevier.

[Tomlinson et al., 2011] Tomlinson, S., Lewis, R., Liu, X., Texier, C., and Carré, M. (2011). Understanding the friction mechanisms between the human finger and flat contacting surfaces in moist conditions. *Tribology Letters*, 41:283–294.

[Van Kuilenburg et al., 2013] Van Kuilenburg, J., Masen, M. A., and Van Der Heide, E. (2013). Contact modelling of human skin: What value to use for the modulus of elasticity? *Proceedings of the institution of mechanical engineers, Part J: Journal of Engineering Tribology*, 227(4):349–361.

[van Kuilenburg et al., 2015] van Kuilenburg, J., Masen, M. A., and van der Heide, E. (2015). A review of fingerpad contact mechanics and friction and how this affects tactile perception. *Proceedings of the Institution of Mechanical Engineers, Part J: Journal of Engineering Tribology*, 229(3):243–258.

[Vodlak et al., 2016] Vodlak, T., Vidrih, Z., Vezzoli, E., Lemaire-Semail, B., and Peric, D. (2016). Multi-physics modelling and experimental validation of electrovibration based haptic devices. *Biotribology*, 8:12–25.

[WA, 1994] WA, W. A. (1994). Biaxial tension test of human skin in vivo. *Bio-Medical Materials and Engineering*, 4(7):473–486.

[Wang et al., 2020] Wang, J., Tiwari, A., Sivebaek, I., and Persson, B. (2020). Sphere and cylinder contact mechanics during slip. *Journal of the Mechanics and Physics of Solids*, 143:104094.

[Wu et al., 2006] Wu, J. Z., Welcome, D. E., and Dong, R. G. (2006). Three-dimensional finite element simulations of the mechanical response of the fingertip to static and dynamic compressions. *Computer Methods in Biomechanics and Biomedical Engineering*, 9(1):55–63.

[Xu et al., 2022] Xu, Y., Scheibert, J., Gadegaard, N., and Mulvihill, D. M. (2022). An asperity-based statistical model for the adhesive friction of elastic nominally flat rough contact interfaces. *Journal of the Mechanics and Physics of Solids*, 164:104878.

[Zhou et al., 2020] Zhou, X., Mo, J. L., Li, Y. Y., Xiang, Z. Y., Yang, D., Masen, M. A., and Jin, Z. M. (2020). Effect of finger sliding direction on tactile perception, friction and dynamics. *Tribology Letters*, 68:1–13.